Restoration of visual function in adult mice with an inherited retinal disease via adenine base editing

Susie Suh[1,2,12,✉], **Elliot H. Choi**[1,2,12], **Henri Leinonen**[1], **Andrzej T. Foik**[3,4], **Gregory A. Newby**[5,6,7], **Wei-Hsi Yeh**[5,6,7,8], **Zhiqian Dong**[1], **Philip D. Kiser**[9,10], **David C. Lyon**[3], **David R. Liu**[5,6,7], **Krzysztof Palczewski**[1,9,11,✉]

[1]Gavin Herbert Eye Institute, Department of Ophthalmology, University of California, Irvine, Irvine, CA, USA [2]Department of Pharmacology, Case Western Reserve University, Cleveland, OH, USA [3]Department of Anatomy and Neurobiology, School of Medicine, University of California, Irvine, Irvine, CA, USA [4]International Centre for Translational Eye Research, Institute of Physical Chemistry, Polish Academy of Sciences, Warsaw, Poland [5]Merkin Institute of Transformative Technologies in Healthcare, Broad Institute of Harvard and MIT, Cambridge, MA, USA [6]Department of Chemistry and Chemical Biology, Harvard University, Cambridge, MA, USA [7]Howard Hughes Medical Institute, Harvard University, Cambridge, MA, USA [8]Program in Speech and Hearing Bioscience and Technology, Harvard Medical School, Boston, MA, USA [9]Department of Physiology and Biophysics, University of California, Irvine, Irvine, CA, USA [10]Research Service, VA Long Beach Healthcare System, Long Beach, CA, USA [11]Department of Chemistry, University of California, Irvine, Irvine, CA, USA [12]These authors contributed equally: Susie Suh, Elliot H. Choi

Abstract

Cytosine base editors and adenine base editors (ABEs) can correct point mutations predictably and independent of Cas9-induced double-stranded DNA breaks (which causes substantial indel formation) and homology-directed repair (which typically leads to low editing efficiency). Here, we show, in adult mice, that a subretinal injection of a lentivirus expressing an ABE and a single-guide RNA targeting a de novo nonsense mutation in the *Rpe65* gene corrects the pathogenic mutation with up to 29% efficiency and with minimal formation of indel and off-target mutations, despite the absence of the canonical NGG sequence as a protospacer-adjacent motif. The ABE-treated mice displayed restored RPE65 expression and retinoid isomerase activity, and near-normal levels of retinal and visual functions. Our findings motivate the further testing of ABEs for the

treatment of inherited retinal diseases and for the correction of pathological mutations with non-canonical protospacer-adjacent motifs.

Leber congenital amaurosis (LCA) is a group of inherited retinal disorders caused by loss-of-function mutations in several genes that are important for retinal function[1]. Most patients with LCA have severe visual impairment throughout infancy or childhood and become legally blind by the third or fourth decade of life due to progressing retinal degeneration[2]. This devastating form of retinal disorder had no treatments available until recent gene therapy development. The US Food and Drug Administration-approved gene therapy is specifically targeted for patients with LCA who have biallelic mutations in the *RPE65* gene[3,4]. The therapeutic strategy is based on the subretinal delivery of a functional *RPE65* complementary DNA (cDNA) copy to the patient's eye using adeno-associated virus (AAV)[3]. Early clinical trials have shown improvements in visual function for the first year, but several long-term reports raised concerns about the continuation of retinal degeneration and declining vision after 1–3 years[5–8]. One of the hypotheses for the fading effect is that the progression of retinal degeneration triggered by RPE-specific 65-kDa protein (RPE65) deficiency may be resistant to subsequent RPE65 augmentation[5,6,8]. Another hypothesis is that the transgene expression level from AAV vectors may decline over time or does not meet the demand for maintenance of retinal health[5,6].

Genome editing with CRISPR–Cas9 technology has great potential to advance the current gene therapy approach, with the ability to correct mutations in the endogenous DNA[9,10]. In the early stage of CRISPR–Cas9 technology, the ability to correct a point mutation was dependent on the rate of homology-directed repair (HDR) following the delivery of wild-type (WT) Cas9, corresponding single-guide RNA (sgRNA) and homologous donor sequence[11]. However, the correction by HDR has shown to be highly ineffective, particularly in non-dividing cells, and the double-stranded DNA break formation by Cas9 nuclease generates substantial numbers of undesired indel mutations that abrogate the potential benefit from corrected mutation[12,13]. Base editors are a class of genome-editing tool that can achieve targeted conversion of a single base pair independent of HDR and double-stranded DNA break formation[14]. There are two types of base editors: cytosine base editors (CBEs, which comprise a catalytically impaired Cas9 (dCas9) with cytidine deaminase (rAPOBEC1)); and adenine base editors (ABEs, which comprise dCas9 with adenosine deaminase (TadA))[15,16]. When introduced into a cell, CBEs and ABEs enable the conversion of C•G to T•A or vice versa with high precision and efficiency[15,16]. Therapeutic applications of base editors have recently been reported in animal models of liver disease[17,18], skin disorder[19] and muscle dystrophy[20], demonstrating the great potential of base editing for the treatment of various genetic disorders.

We hypothesized that base editors can be used to target the mutations associated with inherited retinal diseases. To test our hypothesis, we aimed to correct a de novo nonsense mutation in the *Rpe65* gene on exon 3 (c.130C > T; p.R44X) in the *rd12* mouse model[21] (Fig. 1a). A homologous mutation has recently been identified as an LCA-causing mutation among the Chinese population[22], highlighting the clinical relevance of the animal model. The *rd12* mutation in the mouse abolishes the expression of RPE65, a key isomerase in the

classical visual cycle that regenerates the active visual chromophore 11-*cis*-retinal[21,23]. Therefore, these mice display visual cycle blockade and profoundly impaired visual function. Fortuitously, the production of 11-*cis*-retinal offers a direct biochemical read-out for the phenotypic improvement of gene repair, making the *rd12* mouse model a robust system with which to test genome-editing approaches.

Results

In vitro screening of *Rpe65* base editing.

Gene correction in *rd12* mice using an HDR approach has recently been reported[24] and was evaluated in our previous experiments (Supplementary Fig. 1); however, this approach resulted in a low correction efficiency (~1% in ref. [24]; 0.03% in our experiments) with a higher proportion of indel formation[24]. Furthermore, the HDR strategy did not restore functional RPE65, nor did it improve the disease phenotype in vivo (Supplementary Fig. 1). Given that cells of the retinal pigment epithelium (RPE) are postmitotic and exist in a small population, we concluded that a dual-AAV-mediated HDR approach is not therapeutically viable.

We reasoned that subretinal delivery of ABE would correct the pathological mutation by converting A to G on the complementary strand of the *Rpe65* gene with higher precision and minimal undesired mutations. In previous reports that employed a base editor in other disease models[17,20], the target mutation had the canonical NGG protospacer-adjacent motif (PAM) sequence, whereas the *rd12* mouse model does not contain an NGG PAM sequence properly positioned to correct the mutation[17,20]. To overcome this obstacle, we first tested xCas9(3.7)–ABE (xABE)—an ABE variant fused to an evolved xCas9(3.7), which can recognize a broad range of PAMs—with five different protospacer sequences placing the target A within the activity window of 4–8 (referred to as sgRNA-A4 to sgRNA-A8) (Fig. 1b,d)[25].

To test the base-editing efficacy in vitro, we generated a reporter NIH3T3 cell line by stably integrating *rd12* mutant *Rpe65* cDNA, hereby referred to as the *rd12* cell line (Fig. 1c). We transfected *rd12* cells with xABE and one of each of the sgRNA expression plasmids, and subsequently determined RPE65 expression by western blot analysis 48 h after transfection (Supplementary Fig. 2). Cells transfected with sgRNA-A5 and sgRNA-A6 each showed an RPE65 band at the expected molecular weight, although A5 revealed a more intense band than A6 (Supplementary Fig. 2).

We then sought to bolster the base-editing efficiency by replacing xABE with a codon-optimized ABE variant (ABEmax), which shows enhanced protein expression[26]. Although ABEmax targets DNA with SpCas9 instead of xCas9(3.7), we hypothesized that a higher protein expression level from ABEmax might compensate for its relatively low recognition of non-canonical PAM sites. Furthermore, several lines of evidence from the literature suggest that, in addition to NGG PAM, non-canonical PAMs including NAG and NGA, which coincide with the PAM sites of sgRNA-A5 and -A6, respectively, can be recognized by SpCas9 (refs. [27–29]).

Interestingly, ABEmax indeed showed higher correction efficiency than xABE with both sgRNA-A5 and -A6 (Fig. 1e,f). We reasoned that codon optimization of ABE in ABEmax could have yielded more stable and higher protein expression, leading to more frequent base-editing activity at sites lacking a canonical NGG PAM (Supplementary Fig. 3).

Deep-sequencing analysis on A5- and A6-transfected cells showed correction rates of 2.88 ± 0.19 and $3.43 \pm 0.04\%$, respectively (Fig. 1g). We note that the low correction frequency is probably attributed to multiple factors. First, the integration of multiple copies of viral $Rpe65^{rd12}$ cDNA in each cell may leave some editable sites untargeted by ABEmax. Second, a low transfectability of the $rd12$ cell line may further reduce the probability of co-transfection in each cell. Lastly, the NGG PAM preference of ABEmax might contribute to low base-editing activity at these non-canonical PAM sites, although our experiments demonstrated no remarkable difference in base editing between non-NGG and NGG PAM sites in the $rd12$ cell line (Supplementary Fig. 4).

Nevertheless, a single-base correction of the target mutation ($T_7 > C$) was the most frequent alteration in both A5- and A6-transfected cells. Besides the target base substitution, two other allelic variants were generated by the bystander editing (Fig. 1g). The first variant ($T_5 > C$) introduces a Leu to Pro mutation at amino acid position 43 but maintains the stop codon, resulting in premature truncation (Fig. 1g). The second variant (T_5, $T_7 > C$) corrects the stop codon but also introduces the Leu43Pro change, which expresses non-functional mutant RPE65 without known toxicity (Supplementary Fig. 5). These two variants were observed at higher frequencies in A5-transfected cells ($2.55\% \pm 0.17$ and $1.07\% \pm 0.01\%$, respectively) than in A6-transfected cells ($0.19\% \pm 0.02$ and $0.14\% \pm 0.01\%$, respectively) (Fig. 1g). Besides these conversions, no other DNA modifications, including insertions, deletions and substitutions, were observed above the background level in the non-transfected control group. The sequencing results from in vitro experiments confirmed that ABEmax with both sgRNA-A5 and -A6 can correct the nonsense mutation with minimal indel mutations.

ABE corrects the *Rpe65* mutation in the mouse RPE.

To deliver the sgRNA and ABEmax to the mouse RPE tissue in vivo, we produced three lentiviral vectors, each encoding ABEmax with sgRNA-A5, sgRNA-A6 or non-targeting control sgRNA to serve as a control group (referred to as LV-ABE-A5, LV-ABE-A6 and LV-ABE-NT, respectively) (Fig. 2a). We chose lentiviral over recently described AAV delivery vectors[17,30] to maximize transduction and ABEmax expression and evaluate the greatest possible efficacy of the base-editing approach. Lentivirus also exhibits RPE-specific tropism when injected subretinally to the mouse eye, obviating the need for a tissue-specific promoter[31] (Supplementary Fig. 6).

We injected 4-week-old $rd12$ mice subretinally with LV-ABE-A5, LV-ABE-A6 or LV-ABE-NT (1×10^6 transducing units per eye for each lentivirus) or phosphate-buffered saline (PBS). In each group, we co-injected AAV1-CMV-eGFP (5×10^7 genome copies per eye) to ensure successful delivery by measuring fundus fluorescence using in vivo scanning laser ophthalmoscopy 2 weeks after the injection, and the eyes that had >70% Enhanced green fluorescent protein (eGFP) fluorescence were used for post-treatment analysis. Five weeks

after the injection, we evaluated RPE65 protein restoration in the treated eye by western blot. The RPE lysates from LV-ABE-A5-injected (A5-treated) and LV-ABE-A6-injected (A6-treated) mouse eyes showed the RPE65 band, although it was not as intense as the band from the WT mouse eye (Fig. 2b). Conversely, no RPE65 was detected from the PBS-injected (untreated) and LV-ABE-NT-injected (NT-treated) mouse eyes (Fig. 2b). The correct localization of rescued RPE65 in the RPE tissue layer was also confirmed on the cross-sections of mouse eyes by immunofluorescence analysis (Fig. 2c). To assess the approximate percentage of corrected cells from each eye, RPE tissue was processed as a flatmount and analysed by immunofluorescence, which showed a rescue of 32% in A5-treated eyes and 17% in A6-treated eyes (Fig. 2d,e).

To quantify the correction efficiency, we performed targeted deep sequencing of the DNA isolated from the mouse RPE tissue. We observed target base editing ($T_7 > C$) without any bystander effects at a rate of $15.95 \pm 2.87\%$ in the A5-treated RPE tissue and $5.22 \pm 1.01\%$ in the A6-treated RPE tissue ($n = 8$ eyes in each group) with a maximum correction of up to 29% in A5 and 11% in A6 (Fig. 2f). We note that these numbers are slightly underestimated because the DNA samples from the RPE cells included cells from choroid and sclera, which were not exposed to the virus, from dissections. In contrast, we observed no substantial indel mutation at a rate of $0.48 \pm 0.11\%$ in the A5-treated group and $0.16 \pm 0.01\%$ in the A6-treated group compared with the two control groups: NT treated ($0.11 \pm 0\%$; $n = 4$ eyes) and untreated ($0.14 \pm 0.02\%$; $n = 3$ eyes) (Fig. 2f). To examine other potential bystander editing, we analysed the composition of allelic variants in a representative RPE sample from each treatment group. In both A5 and A6, a single base conversion at the target mutation ($T_7 > C$) was the most frequent allele (Fig. 2g). Two base conversions ($T_7 > C$ and $T_5 > C$) and a single non-target base conversion ($T_5 > C$) were the second and third most frequent alleles in A5, while these frequencies were reversed in A6. Overall, A5 showed a higher frequency of bystander editing than A6, consistent with the sequencing outcome from in vitro experiments.

Off-target analysis of *Rpe65* base editing.

We also assessed the off-target activity of both sgRNA-A5 and -A6 in the RPE tissue by examining the top ten potential off-target sites identified by unbiased, genome-wide circularization for in vitro reporting of cleavage effects by sequencing (CIRCLE-seq)[32] (Supplementary Fig. 7). In both A5- and A6-treated RPE tissues, we did not detect off-target editing above the background level of the untreated RPE tissue, corresponding with the previous finding showing a low off-target activity of ABE[33,34]. With low off-target activity in both sgRNAs, sgRNA-A5 showed higher on-target base-editing efficiency, although sgRNA-A6 demonstrated higher precision with less bystander editing activity. To further evaluate the therapeutic effects from base editing, we decided to assess the visual function in A5-treated mice, given their higher correction efficiency.

Base editing restores the visual chromophore in *rd12* mice.

We evaluated whether a functional visual cycle can be restored in A5-treated *rd12* mice. In a classical visual cycle, RPE65 isomerizes all-*trans*-retinyl esters into 11-*cis*-retinol, which is an essential biochemical reaction for regeneration of the visual chromophore, 11-*cis*-

retinal[35] (Fig. 3a). In *rd12* mice, this visual cycle is blocked due to the absence of RPE65, resulting in an extreme 11-*cis*-retinal deficiency and accumulation of all-*trans*-retinyl esters[21]. In retinoid analysis by high-performance liquid chromatography (HPLC), the A5-treated *rd12* mouse eyes revealed substantial production of 11-*cis*-retinal after full dark adaptation (constituting 30% of the WT level) and 34% reduction of all-*trans*-retinyl esters compared with the NT-treated control group, indicating a restored visual cycle (Fig. 3b and Supplementary Fig. 8a–c). Furthermore, we confirmed that the new supply of 11-*cis*-retinal can photoisomerize to all-*trans*-retinal immediately following a flash stimulus (Fig. 3c).

Base editing rescues retinal and visual function in mice.

Next, we determined whether visual chromophore recovery can restore the function of different cell types comprising the primary visual pathways in A5-treated mice (Fig. 3d). First, we assessed retinal cell activity by scotopic electroretinography (ERG). This technique allows functional assessment of photoreceptors and downstream retinal interneurons through information encoded in the a wave and b wave, respectively[36]. Both untreated and NT-treated *rd12* mice exhibited a complete absence of a- and b-wave amplitudes in response to an intermittent flash stimulus of -0.3 log[cd s m^{-2}], whereas A5-treated mice recovered average a- and b-wave amplitudes of 44 and 65% of the WT control responses (Fig. 3e,f).

We then assessed the optomotor responses (OMRs) mediated by the superior colliculus, which is the most prominent target of the retinal projection in mice[37]. In mice, more than 70% of retinal ganglion cell axons project to the superficial layers of the superior colliculus, and the remaining 30% project to the primary visual cortex (V1) via the dorsal lateral geniculate nucleus[38,39]. Therefore, the OMR test provides a robust means of evaluating the functional integrity of the visual pathway in mice[37]. The quantitative OMR test measures visual function by quantifying the animal's reflexive head movements in response to rotating stripes[40] (Fig. 3g). In moderate ambient luminance of ~1 lux (that is, low twilight light level), both WT and A5-treated *rd12* mice showed a tracking response starting from 5% contrast between the white and black sinusoidal gratings (Fig. 3h,i). In contrast, untreated and NT-treated *rd12* mice did not show tracking behaviour, even for the highest-contrast stimuli of 50%.

Recovery of visual cortical responses in the treated mice.

Lastly, we evaluated whether base-editing treatment can restore the functional integrity of the visual pathway from the retina to the primary visual cortex (V1) and the cortical processing of visual information. We recorded both visually evoked potentials (VEPs), which represent the global electrical response of V1 (Fig. 4a–d), and single V1 neuron activity, which represents the functional quality of individual cortical cells (Fig. 4e–g). In VEP recordings, A5-treated mice showed substantial recovery of normalized VEP amplitudes (1.91 ± 0.29 µV) that constituted 70% of that found in WT mice (2.75 ± 0.27 µV) (Fig. 4c), although the response latency was longer than that for the WT mice (0.13 s in A5 versus 0.07 s in WT) (Fig. 4d). In contrast, we did not observe VEP amplitudes above the noise signal from either untreated (0.20 ± 0.02 µV) or NT-treated (0.31 ± 0.03 µV) *rd12* mice (Fig. 4c).

In single-neuron recordings, a predominant proportion of V1 neurons from the A5-treated mice had light-evoked responses (93.8% in A5 compared with 95.2% in WT), whereas not a single cell with visual responses was detected from untreated and NT-treated *rd12* mice (Fig. 4e,g). Furthermore, A5-treated mice not only had near-normal firing rates (Fig. 4f), but also showed strong selective responses to various stimulus parameters, such as orientation, spatial and temporal frequency, receptive field size and contrast (Fig. 5a–e and Supplementary Fig. 9).

Discussion

In this proof-of-concept study, we provide evidence of the clinical potential of base editors for the correction of mutations causing inherited retinal diseases and for restoring visual function. After we optimized the base-editing outcome using an in vitro system, we translated the base-editing strategy to a mouse model and showed a substantial level of vision restoration. We used the lentiviral vector for this initial proof-of-concept study, recognizing that safer alternative delivery methods, such as split intein–AAV vectors[17,30], will need to be optimized for translation to the clinic. Additionally, the efficacy and safety profile of each sgRNA must be thoroughly assessed for each disease condition. Nevertheless, our study provides a framework for the preclinical development of a base-editing therapeutic for other inherited retinal diseases caused by different mutations.

Although we showed the base editing of a specific nonsense mutation in the *Rpe65* gene, we envision that a majority of other inherited retinal disease-associated mutations could be corrected by choosing another sgRNA that accommodates the desired mutation and applying a newly developed base editor variant that can recognize various PAM sites[41,42]. Recently, a wide variety of engineered base editor variants have been described (including SpCas9-NRRH, -NRCH, -NRTH, -NG, -NY and -NR) that are no longer practically constrained by the requirement of PAM for sequence recognition and enable base editing of a previously inaccessible pathogenic single-nucleotide polymorphism[41,42]. Using the set of engineered base editor variants, we can theoretically correct up to 95% of all transition mutations or 62% of all point mutations associated with human disease[41,43], supporting the clinical utility of base-editing treatment for diverse forms of inherited retinal diseases.

Gene therapy approaches to treating inherited retinal diseases are of special interest given the accessibility of the eye, its immune-privileged status and the successful clinical trials of *RPE65* gene augmentation therapy that led to the first US Food and Drug Administration-approved gene therapy[3]. This landmark therapeutic advance was made possible through the work of numerous laboratories in the United States and England[4,44–46]. Now, as demonstrated in this study, base-editing technology can provide an alternative treatment model of gene augmentation therapy to permanently rescue the function of a key vision-related protein disabled by mutations, or to correct dominant alleles for which gene augmentation may not be effective. This work represents an advance towards the development of treatments for inherited retinal diseases.

Methods

Mice.

The pigmented *rd12* mice and C57BL/6J mice were purchased from The Jackson Laboratory (005379 and 000664, respectively). All mice were housed in the vivarium at the University of California, Irvine, where they were maintained on a normal mouse chow diet and a 12 h/12 h light/dark cycle. All animal procedures were approved by the Institutional Animal Care and Use Committee of the University of California, Irvine, and were conducted in accordance with the Association for Research in Vision and Ophthalmology Statement for the Use of Animals in Ophthalmic and Visual Research.

Cell line generation.

NIH3T3-RPE65 (WT) and NIH3T3-RPE65 (*rd12*) stable cell lines were generated by transduction of NIH3T3 cells with retrovirus obtained from Phoenix-Eco cells transfected with either pMXs-RPE65(WT)-IRES-GFP or pMXs-RPE65(*rd12*)-IRES-GFP according to a previously published protocol[47]. Transduced cells were sorted by a FACSAria cell sorter (BD Biosciences) to selectively collect transduced cells and ensure comparable GFP expression between NIH3T3-RPE65 (WT) and NIH3T3-RPE65 (*rd12*). To make RPE65 expression vectors, WT or *rd12* mouse Rpe65 cDNA sequences, flanked by *EcoRI* and *NotI*, were purchased from Gene Universal and cloned into the multiple cloning site of pMXs-IRES-GFP (a gift from T. Kitamura at the University of Tokyo)[48]. The downstream sequence of the internal ribosomal entry site (IRES) and GFP allows co-expression of RPE65 and GFP, thereby enabling cell sorting by flow cytometry. Cells were maintained in growth medium composed of Dulbecco's modified Eagle's medium (Gibco; 11965084) supplemented with 10% (vol/vol) heat-inactivated foetal bovine serum (Thermo Fisher; A3840001) and 1% (vol/vol) Penicillin/Streptomycin mix (Thermo Fisher; 151401122). Cells were maintained at 37 °C in 5% CO_2.

Construction of ABEmax and sgRNA expression plasmids for in vitro base-editing validation.

pCMV-ABEmax (Addgene; plasmid 112095)[26] and xCas9(3.7)–ABE(7.10) (Addgene; plasmid 108382)[25] were used to express ABEmax and xABE, respectively. For U6-sgRNA expression plasmids, five different sgRNA oligonucleotides were synthesized (Genewiz) and cloned into the pSPgRNA vector (a gift from C. Gersbach; Addgene; 47108)[49] using the BbsI restriction site. The primers used for cloning are listed in Supplementary Table 2.

Virus production for in vivo delivery of ABE agents.

To generate a single lentiviral construct co-expressing sgRNA and ABEmax, the U6-sgRNA cassette was PCR amplified from the previously made sgRNA expression plasmids with the primers including restriction sites MluI and BcuI, and cloned into the compatible restriction sites in the pCMV-ABEmax plasmid. For the non-targeting sgRNA, the sgRNA sequence was derived from the GeCKO v2 mouse sgRNA library and the gene fragment comprising U6-sgRNA was synthesized by Genewiz for subsequent cloning. The resulting U6-sgRNA-CMV-ABEmax plasmid was subsequently cloned into the third-generation lentiviral transfer

vector, LentiCRISPRv2GFP (a gift from D. Feldser; Addgene; 82416)[50], replacing the transgene sequences between the 5′ and 3′ long terminal repeat sequences. The final cloned plasmids were packaged into lentivirus particles by SignaGen (these sequences are available in Supplementary Table 3). AAV1-CMV-eGFP (Addgene; viral prep 105545-AAV1), serving as a fluorescence marker, was purchased from Addgene.

Plasmid transfection for in vitro base-editing validation.

NIH3T3-RPE65 (*rd12*) cells were seeded on a 24-well plate 18 h before transfection. At ~70% confluency, cells were transfected with 750 ng ABEmax or xABE plasmid and 250 ng sgRNA plasmid using 1.5 μl Lipofectamine 3000 (Thermo Fisher; L3000001) per well.

Off-target analysis using CIRCLE-seq.

CIRCLE-seq was performed as previously described[32]. Genomic DNA from a C57/BL6 mouse was isolated from liver tissue using a Gentra Puregene Tissue Kit (Qiagen; 158667). PCR amplification before sequencing was conducted using PhusionU polymerase (New England Biolabs; M0530S), and products were gel-purified and quantified with a Qubit High-Sensitivity Kit (Thermo Fisher; Q33230) before loading onto an Illumina MiSeq. Data were processed using the CIRCLE-seq analysis pipeline with the following parameters: Read_threshold: 4; window_size: 3; mapq_threshold: 50; start_threshold: 1; gap_threshold: 3; mismatch_threshold: 6; mIllued_analysis: True.

Deep-targeted sequencing analysis.

Genomic DNA from cultured cells or mouse RPE tissue was isolated using the DNeasy Blood and Tissue Kit (Qiagen; 69504) according to the manufacturer's instructions. Following DNA isolation, 265- to 308-base pair PCR amplicons of on- and off-target predicted sites for *Rpe65* were generated using primers with partial Illumina adapter sequences and then purified using the QIAquick PCR Purification Kit (Qiagen; 28106). Samples were sequenced on an Illumina MiSeq by Genewiz. Between 70,000 and 100,000 next-generation sequencing reads for each sample were generated on 2×250 base pair paired-end reads. The primers used for on-target and off-target analysis are listed in Supplementary Table 4. Excel 2016 was used to calculate means and s.e.m. values from each group. SigmaPlot 14 was used for making graphs.

Mouse subretinal injection.

Mice were anaesthetized by intraperitoneal injection of a cocktail consisting of 20 mg ml^{-1} ketamine and 1.75 mg ml^{-1} xylazine in PBS at a dose of 0.1–0.13 ml per 25 g body weight, and their pupils were dilated with topical administration of 1% tropicamide ophthalmic solution (Akorn; 17478-10212). Subretinal injections were performed using an ophthalmic surgical microscope (Zeiss). An incision was made through the cornea adjacent to the limbus at the nasal side using a 26-gauge needle. A 35-gauge blunt-end needle (World Precision Instruments; NF35BL-2), connected to an RPE-KIT (World Precision Instruments) by SilFlex tubing (World Precision Instruments; SILFLEX-2), was inserted through the corneal incision while avoiding the lens and pushed through the retina. Each mouse received 1 μl injection compound per eye.

HPLC retinoid profiling in the mouse eye.

Mice were adapted to the dark for 2 d before the enucleation of the eyes. The retinoid analysis of light-exposed mouse eyes included a 0.5-s flash exposure from a 30-cm distance before eye enucleation. Two eyes from WT, untreated and treated *rd12* mice were homogenized in 10 mM sodium phosphate buffer (pH 8.0) containing 50% methanol (vol/vol) (Sigma–Aldrich; 34860-1L-R) and 100 mM hydroxylamine (Sigma–Aldrich; 159417-100G). After 15 min incubation at room temperature, 2 ml 3 M sodium chloride was added. The resulting sample was extracted twice with 3 ml ethyl acetate (Fisher Scientific; E195-4). Then, the combined organic phase was dried in vacuo and reconstituted in 300 µl hexane. Extracted retinoids (100 µl were separated on a normal-phase HPLC column (Sil; 5 µm 4.6 mm × 250 mm; Agilent Technologies) equilibrated with a stepwise gradient of 0.6% ethyl acetate in hexane (Fisher Scientific; H302-4) at an isocratic flow rate of 1.4 ml min^{-1} for 17 min and 10% ethyl acetate in hexane at an isocratic flow rate of 1.4 ml min^{-1} for 25 min. Retinoids were detected by monitoring their absorbance at 325 nm on Agilent ChemStation.

Western blot analysis.

To prepare the protein lysate from transfected cells, each well of cells was lysed in 40 µl ice-cold RIPA buffer (Cell Signaling Technology; 9806S) with protease inhibitors (Sigma–Aldrich; 4693159001) by maintaining constant agitation for 30 min at 4 °C. The lysates were centrifuged for 30 min at 20,000g and 4 °C and the supernatant was saved for gel loading. To prepare the protein lysate from the mouse RPE tissue, the dissected mouse eyecup, consisting of RPE, choroid and sclera, was transferred to a microcentrifuge tube containing 30 µl RIPA buffer with protease inhibitors, and homogenized with a motor tissue grinder (Fisher Scientific; K749540-0000) and centrifuged for 30 min at 20,000g and 4 °C. The resulting supernatant was pre-cleared with Dynabeads Protein G (Thermo Fisher; 10003D) to remove contaminants from the blood before gel loading. Then, 20 µl *rd12* cell lysates (15 µl for RPE lysates) were mixed with NuPAGE LDS Sample Buffer (Thermo Fisher; NP0007) and NuPAGE Sample Reducing Agent (Thermo Fisher; NP0004) and incubated at 70 °C for 10 min, then separated using a NuPAGE 4–12% Bis-Tris gel (Thermo Fisher; NP0321BOX) and transferred onto PVDF membrane (Millipore; IPVH00010), followed by 1 h blocking in 5% (wt/vol) non-fat milk in PBS containing 0.1% (vol/vol) Tween 20 (PBS-T). The membrane was incubated with primary antibody diluted in 1% (wt/vol) non-fat milk in PBS-T overnight at 4 °C. The primary antibodies included: mouse anti-RPE65 monoclonal antibody (1:1,000; in-house production)[51]; mouse anti-Cas9 monoclonal antibody (1:1,000; Invitrogen; MA1-201); rabbit anti-β-actin polyclonal antibody (1:1,000; Cell Signaling Technology; 4970S); and rabbit anti-α-tubulin polyclonal antibody (1:1,000; Cell Signaling Technology; 2144S). After overnight incubation, the membranes were washed three times with PBS-T for 5 min each and then incubated with secondary antibody for 1 h at room temperature. The secondary antibodies included: goat anti-mouse IgG-HRP antibody (1:5,000; Cell Signaling Technology; 7076S); and goat anti-rabbit IgG-HRP antibody (1:5,000; Cell Signaling Technology; 7074S). After washing the membrane three times with PBS-T for 5 min each, protein bands were visualized using the Odyssey Fc imaging system (LI-COR) after exposure to SuperSignal West Pico Chemiluminescent Substrate (Thermo Fisher; 34580).

Immunocytochemistry.

Cells were fixed, permeabilized and blocked using an Image-iT Fixation/Permeabilization Kit, following the manufacturer's protocol (Thermo Fisher; R37602). Cells were immunostained with mouse anti-RPE65 monoclonal antibody (1:1,000) and rabbit anti-GRP78 BiP polyclonal antibody (1:1,000; Abcam; ab21685) diluted in PBS-T, followed by the corresponding Alexa Fluor 555 goat anti-mouse IgG (1:1,000; Thermo Fisher; A-21424), Alexa Fluor 647 goat anti-rabbit IgG (1:1,000; Thermo Fisher; A-21245) and 4′,6-diamidino-2-phenylindole (DAPI; Thermo Fisher; 62248). Samples were mounted in ProLong Gold antifade reagent (Thermo Fisher; P10144) and imaged at 60× magnification with a Keyence BZ-X810 All-in-One Fluorescence Microscope (Keyence).

Immunohistochemistry of RPE flatmounts and cryosections.

Mouse eyes were fixed with 4% paraformaldehyde in PBS (Santa Cruz Biotechnology; 30525-89-4) for 20 min at room temperature and washed three times in PBS for 5 min each. To make RPE flatmounts (RFMs), the anterior segment and retina were removed from the posterior eyecup under a dissecting microscope, and four radial cuts were made toward the optic nerve to flatten the eyecup into an RFM. To make cryosections, fixed eyes were dehydrated with 30% sucrose in PBS, embedded in O.C.T. (Sakura; 4583) and then flash frozen for cryosectioning at 10-μm thickness. The following procedures are applicable for both RFMs and cryosections. Samples were permeabilized in 0.5% Triton X-100 (Sigma–Aldrich; T8532) in PBS for 30 min, blocked in 3% BSA in PBS for 30 min and incubated with the appropriate primary antibody, including mouse anti-RPE65 antibody (1:100) and rabbit anti-ZO-1 polyclonal antibody (1:100; Invitrogen; 61-7300), overnight at 4 °C. The next day, samples were washed three times in PBS for 5 min each and then incubated with secondary antibody, Alexa Fluor 594-conjugated goat anti-mouse IgG (1:200; Thermo Fisher; A11032) and Alexa Fluor 647-conjugated goat anti-rabbit IgG (1:200; Thermo Fisher) for 2 h at room temperature in the dark. The samples were incubated in 1 μg ml^{-1} DAPI (Thermo Fisher; 62248) in PBS for 10 min and washed three times in PBS for 5 min each. The samples were then mounted with ProLong Gold mounting media and imaged as described above. For quantification of RPE65$^+$ cells in Fig. 2e, ten images were taken from different areas of the RFM using a TxRed filter at 40× magnification. The analysis was performed using ImageJ. All images were converted to RGB stack, then the bottom and top thresholds were set using the control and WT groups. The percentage of positive signal from each image was automatically calculated by applying the established threshold.

ERG.

Before recording, mice were adapted to the dark for 24 h. Under a safety light, mice were anaesthetized by intraperitoneal injection of a cocktail consisting of 20 mg ml^{-1} ketamine and 1.75 mg ml^{-1} xylazine in PBS at a dose of 0.1–0.13 ml per 25 g body weight. Pupils were dilated with 1% tropicamide (Henry Schein; 1127192), then 2.5% hypromellose (Akorn; 9050-1) was applied to keep the corneas hydrated and to facilitate electrical conductivity. Active recording electrodes were placed onto the corneas and reference and ground electrodes were positioned subdermally (between the ears and on the tail, respectively). The eyes were stimulated with a green light (peak emission = 544 nm;

bandwidth = ~160 nm) stimulus of –0.3 log[cd s m^{-2}]. The responses for ten stimuli with an inter-stimulus interval of 10 s were averaged and the a- and b-wave responses were acquired from the averaged ERG waveform. The a wave is the first negative polarity deflection after stimulus onset, and the b wave is the first positive peak occurring after the a-wave trough. The ERGs were recorded with the Celeris rodent electrophysiology system (Diagnosys) and analysed with Espion version 6 software (Diagnosys). SigmaPlot 14 was used to create the graphs and perform statistical analysis.

OMR test.

OMRs were assessed using a commercial OMR platform that utilizes automated head tracking and behaviour analysis (PhenoSys). The software automatically compares horizontal head movement in relation to the speed of a moving vertical grating stimulus and quantifies correct/incorrect tracking behaviour. The OMR arena was dimmed using neutral density filters in front of the stimulus displays. The ambient luminance was measured at ~1 lux, corresponding to a mesopic, roughly twilight light level. When a light-adapted mouse was placed on the OMR arena's elevated platform, rotating ($12° s^{-1}$) vertical sinusoidal grating stimuli were presented for 10 min per trial. The spatial frequency of the grating was set at 0.1 cycles per degree of the visual angle. This stimulus was presented at differing contrasts between the light and dark: 5, 7.5, 10, 12.5, 15, 17.5, 20, 25, 50 and 100% contrast. Stimulation at each contrast level lasted 60 s and contrast levels were presented in a randomized order, except that each session was always started with 100% contrast stimuli, the results for which were omitted from the analysis due to mouse acclimatization. Each mouse was tested in at least four trials (maximum two trials per day) and the first 10-min trial was considered acclimatization and not used in the analysis. The performances of the remaining rest trials were averaged for analysis, excluding those 60-s stimulus periods that led to a correct/incorrect ratio smaller than 0.8. SigmaPlot 14 was used to create the graphs and perform statistical analysis.

Primary visual cortex (V1) electrophysiology.

Mice were initially anaesthetized with 2% isoflurane in a mixture of N_2O/O_2 (70%/30%) then placed into a stereotaxic apparatus. A small, custom-made plastic chamber was glued to the exposed skull. One day after recovery, re-anaesthetized animals were placed in a custom-made hammock, maintained under isoflurane anaesthesia (1–2% in a mixture of N_2O/O_2), and four individual tungsten electrodes were inserted into a small craniotomy above the visual cortex of the right hemisphere. Once electrodes were inserted, the chamber was filled with sterile agar. During recording sessions, animals were sedated with chlorprothixene hydrochloride (1 mg kg^{-1}; intramuscular) and kept under light isoflurane anaesthesia (0.2–0.4%). Electroencephalogram and electrocardiogram outputs were monitored throughout the experiments, and body temperature was maintained with a heating pad (Harvard Apparatus).

Data were acquired using a 32-channel Scout recording system (Ripple). The local field potential from multiple locations was bandpass filtered from 0.1 to 250 Hz and stored together with spiking data on a computer with a 1-kHz sampling rate. The local field potential signal was cut according to stimulus time stamps and averaged across trials for each recording location to calculate VEPs[52]. The spike signal was bandpass filtered from

500 to 7 kHz and stored in a computer hard drive at a 30-kHz sampling frequency. Spikes were sorted online in Trellis (Ripple) while performing visual stimulation. Visual stimuli were generated in MATLAB (MathWorks) using the Psychophysics Toolbox and displayed on a gamma-corrected liquid-crystal display monitor[53] (140 cm; 60 Hz; 1,920 pixels × 1,080 pixels; 52 cd m^{-2} mean luminance). Stimulus onset times were corrected for liquid-crystal display monitor delay using a photodiode and microcontroller[54] (in-house design).

For recordings of visually evoked single-cell responses, the eyes were first stimulated with 100 repetitions of a 500-ms bright flash (105 cd m^{-2}). Receptive fields for visually responsive cells were then located using square-wave drifting gratings, after which optimal orientation/direction and spatial and temporal frequencies were determined using sine wave gratings. The spatial frequencies tested ranged between 0.001 and 0.5 cycles per degree of visual angle. The temporal frequencies tested were 0.1–10 cycles per second. With these optimal parameters, size tuning was assessed using apertures of 1–110° at 100% contrast. With the optimal size and temporal and spatial frequencies, and at high contrast, the orientation selectivity of the cell was tested again using 16 directions at 22.5° increments. This was followed by testing contrast.

Statistics.

The statistical tests used for each experiment are stated in the corresponding figure captions. In vitro experiments were repeated independently at least three times with similar results, as shown in Fig. 1c,e,f and Supplementary Figs. 1c, 2b, 3a and 5b. The experiments in Fig. 2b–d and Supplementary Figs. 1d, g and 6a–c were performed in at least three biologically independent animals and similar results were observed, although not every image was recorded.

Reporting Summary.

Further information on research design is available in the Nature Research Reporting Summary linked to this article.

Data availability

The main data supporting the results of this study are available within the paper and its Supplementary Information. The deep-sequencing data are available from the Sequence Read Archive under accession number PRJNA644016.

Supplementary Material

Refer to Web version on PubMed Central for supplementary material.

Acknowledgements

References

1. Cremers FP, van den Hurk JA & den Hollander AI Molecular genetics of Leber congenital amaurosis. Hum. Mol. Genet. 11, 1169–1176 (2002). [PubMed: 12015276]

2. Den Hollander AI, Roepman R, Koenekoop RK & Cremers FPM Leber congenital amaurosis: genes, proteins and disease mechanisms. Prog. Retin. Eye Res. 27, 391–419 (2008). [PubMed: 18632300]

3. Miraldi Utz V, Coussa RG, Antaki F & Traboulsi EI Gene therapy for *RPE65*-related retinal disease. Ophthalmic Genet. 39, 671–677 (2018). [PubMed: 30335549]

4. Maguire AM et al. Efficacy, safety, and durability of voretigene neparvovec-rzyl in *RPE65* mutation-associated inherited retinal dystrophy: results of phase 1 and 3 trials. Ophthalmology 126, 1273–1285 (2019). [PubMed: 31443789]

5. Bainbridge JW et al. Long-term effect of gene therapy on Leber's congenital amaurosis. N. Engl. J. Med. 372, 1887–1897 (2015). [PubMed: 25938638]

6. Jacobson SG et al. Improvement and decline in vision with gene therapy in childhood blindness. N. Engl. J. Med. 372, 1920–1926 (2015). [PubMed: 25936984]

7. Cideciyan AV et al. Human retinal gene therapy for Leber congenital amaurosis shows advancing retinal degeneration despite enduring visual improvement. Proc. Natl Acad. Sci. USA 110, E517–E525 (2013). [PubMed: 23341635]

8. Gardiner KL et al. Long-term structural outcomes of late-stage *RPE65* gene therapy. Mol. Ther. 28, 266–278 (2020). [PubMed: 31604676]

9. Hsu PD, Lander ES & Zhang F Development and applications of CRISPR–Cas9 for genome engineering. Cell 157, 1262–1278 (2014). [PubMed: 24906146]

10. Doudna JA & Charpentier E The new frontier of genome engineering with CRISPR-Cas9. Science 346, 1258096 (2014). [PubMed: 25430774]

11. Chapman JR, Taylor MR & Boulton SJ Playing the end game: DNA double-strand break repair pathway choice. Mol. Cell 47, 497–510 (2012). [PubMed: 22920291]

12. Lin S, Staahl BT, Alla RK & Doudna JA Enhanced homology-directed human genome engineering by controlled timing of CRISPR/Cas9 delivery. eLife 3, e04766 (2014). [PubMed: 25497837]

13. Cox DB, Platt RJ & Zhang F Therapeutic genome editing: prospects and challenges. Nat. Med. 21, 121–131 (2015). [PubMed: 25654603]

14. Rees HA & Liu DR Base editing: precision chemistry on the genome and transcriptome of living cells. Nat. Rev. Genet. 19, 770–788 (2018). [PubMed: 30323312]

15. Gaudelli NM et al. Programmable base editing of A•T to G•C in genomic DNA without DNA cleavage. Nature 551, 464–471 (2017). [PubMed: 29160308]

16. Komor AC, Kim YB, Packer MS, Zuris JA & Liu DR Programmable editing of a target base in genomic DNA without double-stranded DNA cleavage. Nature 533, 420–424 (2016). [PubMed: 27096365]

17. Villiger L et al. Treatment of a metabolic liver disease by in vivo genome base editing in adult mice. Nat. Med. 24, 1519–1525 (2018). [PubMed: 30297904]

18. Rossidis AC et al. In utero CRISPR-mediated therapeutic editing of metabolic genes. Nat. Med. 24, 1513–1518 (2018). [PubMed: 30297903]

19. Osborn MJ et al. Base editor correction of *COL7A1* in recessive dystrophic epidermolysis bullosa patient-derived fibroblasts and iPSCs. J. Invest. Dermatol. 140, 338–347 (2020). [PubMed: 31437443]

20. Ryu S-M et al. Adenine base editing in mouse embryos and an adult mouse model of Duchenne muscular dystrophy. Nat. Biotechnol. 36, 536–539 (2018). [PubMed: 29702637]

21. Pang JJ et al. Retinal degeneration 12 (rd12): a new, spontaneously arising mouse model for human Leber congenital amaurosis (LCA). Mol. Vis. 11, 152–162 (2005). [PubMed: 15765048]

22. Zhong Z et al. Seven novel variants expand the spectrum of *RPE65*-related Leber congenital amaurosis in the Chinese population. Mol. Vis. 25, 204–214 (2019). [PubMed: 30996589]

23. Redmond TM et al. *Rpe65* is necessary for production of 11-*cis*-vitamin A in the retinal visual cycle. Nat. Genet. 20, 344–351 (1998). [PubMed: 9843205]

24. Jo DH et al. CRISPR–Cas9-mediated therapeutic editing of *Rpe65* ameliorates the disease phenotypes in a mouse model of Leber congenital amaurosis. Sci. Adv. 5, eaax1210 (2019). [PubMed: 31692906]

25. Hu JH et al. Evolved Cas9 variants with broad PAM compatibility and high DNA specificity. Nature 556, 57–63 (2018). [PubMed: 29512652]

26. Koblan LW et al. Improving cytidine and adenine base editors by expression optimization and ancestral reconstruction. Nat. Biotechnol. 36, 843–846 (2018). [PubMed: 29813047]

27. Hsu PD et al. DNA targeting specificity of RNA-guided Cas9 nucleases. Nat. Biotechnol. 31, 827–832 (2013). [PubMed: 23873081]

28. Jiang W, Bikard D, Cox D, Zhang F & Marraffini LA RNA-guided editing of bacterial genomes using CRISPR–Cas systems. Nat. Biotechnol. 31, 233–239 (2013). [PubMed: 23360965]

29. Zhang Y et al. Comparison of non-canonical PAMs for CRISPR/Cas9-mediated DNA cleavage in human cells. Sci. Rep. 4, 5405 (2014). [PubMed: 24956376]

30. Levy JM et al. Cytosine and adenine base editing of the brain, liver, retina, heart and skeletal muscle of mice via adeno-associated viruses. Nat. Biomed. Eng 4, 97–110 (2020). [PubMed: 31937940]

31. Puppo A et al. Retinal transduction profiles by high-capacity viral vectors. Gene Ther. 21, 855–865 (2014). [PubMed: 24989814]

32. Tsai SQ et al. CIRCLE-seq: a highly sensitive in vitro screen for genome-wide CRISPR–Cas9 nuclease off-targets. Nat. Methods 14, 607–614 (2017). [PubMed: 28459458]

33. Xin H, Wan T & Ping Y Off-targeting of base editors: BE3 but not ABE induces substantial off-target single nucleotide variants. Signal Transduct. Target. Ther 4, 9 (2019). [PubMed: 30993016]

34. Jin S et al. Cytosine, but not adenine, base editors induce genome-wide off-target mutations in rice. Science 364, 292–295 (2019). [PubMed: 30819931]

35. Kiser PD, Golczak M & Palczewski K Chemistry of the retinoid (visual) cycle. Chem. Rev. 114, 194–232 (2014). [PubMed: 23905688]

36. Benchorin G, Calton MA, Beaulieu MO & Vollrath D Assessment of murine retinal function by electroretinography. Bio Protoc. 7, e2218 (2017).

37. Leinonen H & Tanila H Vision in laboratory rodents—tools to measure it and implications for behavioral research. Behav. Brain Res. 352, 172–182 (2018). [PubMed: 28760697]

38. Hofbauer A & Dräger UC Depth segregation of retinal ganglion cells projecting to mouse superior colliculus. J. Comp. Neurol. 234, 465–474 (1985). [PubMed: 3988995]

39. Wang L, Sarnaik R, Rangarajan K, Liu X & Cang J Visual receptive field properties of neurons in the superficial superior colliculus of the mouse. J. Neurosci. 30, 16573–16584 (2010). [PubMed: 21147997]

40. Kretschmer F, Sajgo S, Kretschmer V & Badea TC A system to measure the optokinetic and optomotor response in mice. J. Neurosci. Methods 256, 91–105 (2015). [PubMed: 26279344]

41. Miller SM et al. Continuous evolution of SpCas9 variants compatible with non-G PAMs. Nat. Biotechnol. 38, 471–481 (2020). [PubMed: 32042170]

42. Walton RT, Christie KA, Whittaker MN & Kleinstiver BP Unconstrained genome targeting with near-PAMless engineered CRISPR-Cas9 variants. Science 368, 290–296 (2020). [PubMed: 32217751]

43. Lee C et al. CRISPR-pass: gene rescue of nonsense mutations using adenine base editors. Mol. Ther. 27, 1364–1371 (2019). [PubMed: 31164261]

44. Acland GM et al. Gene therapy restores vision in a canine model of childhood blindness. Nat. Genet. 28, 92–95 (2001). [PubMed: 11326284]

45. Acland GM et al. Long-term restoration of rod and cone vision by single dose rAAV-mediated gene transfer to the retina in a canine model of childhood blindness. Mol. Ther. 12, 1072–1082 (2005). [PubMed: 16226919]

46. Jacobson SG et al. Safety of recombinant adeno-associated virus type 2–RPE65 vector delivered by ocular subretinal injection. Mol. Ther. 13, 1074–1084 (2006). [PubMed: 16644289]

47. Chelstowska S, Widjaja-Adhi MAK, Silvaroli JA & Golczak M Impact of LCA-associated E14L LRAT mutation on protein stability and retinoid homeostasis. Biochemistry 56, 4489–4499 (2017). [PubMed: 28758396]

48. Kitamura T et al. Retrovirus-mediated gene transfer and expression cloning: powerful tools in functional genomics. Exp. Hematol. 31, 1007–1014 (2003). [PubMed: 14585362]

49. Perez-Pinera P et al. RNA-guided gene activation by CRISPR–Cas9-based transcription factors. Nat. Methods 10, 973–976 (2013). [PubMed: 23892895]

50. Walter DM et al. Systematic in vivo inactivation of chromatin-regulating enzymes identifies Setd2 as a potent tumor suppressor in lung adenocarcinoma. Cancer Res. 77, 1719–1729 (2017). [PubMed: 28202515]

51. Golczak M, Kiser PD, Lodowski DT, Maeda A & Palczewski K Importance of membrane structural integrity for RPE65 retinoid isomerization activity. J. Biol. Chem. 285, 9667–9682 (2010). [PubMed: 20100834]

52. Foik AT et al. Retinal origin of electrically evoked potentials in response to transcorneal alternating current stimulation in the rat. Invest. Ophthalmol. Vis. Sci. 56, 1711–1718 (2015). [PubMed: 25650414]

53. Brainard DH The psychophysics toolbox. Spat. Vis. 10, 433–436 (1997). [PubMed: 9176952]

54. Foik AT et al. Detailed visual cortical responses generated by retinal sheet transplants in rats with severe retinal degeneration. J. Neurosci. 38, 10709–10724 (2018). [PubMed: 30396913]
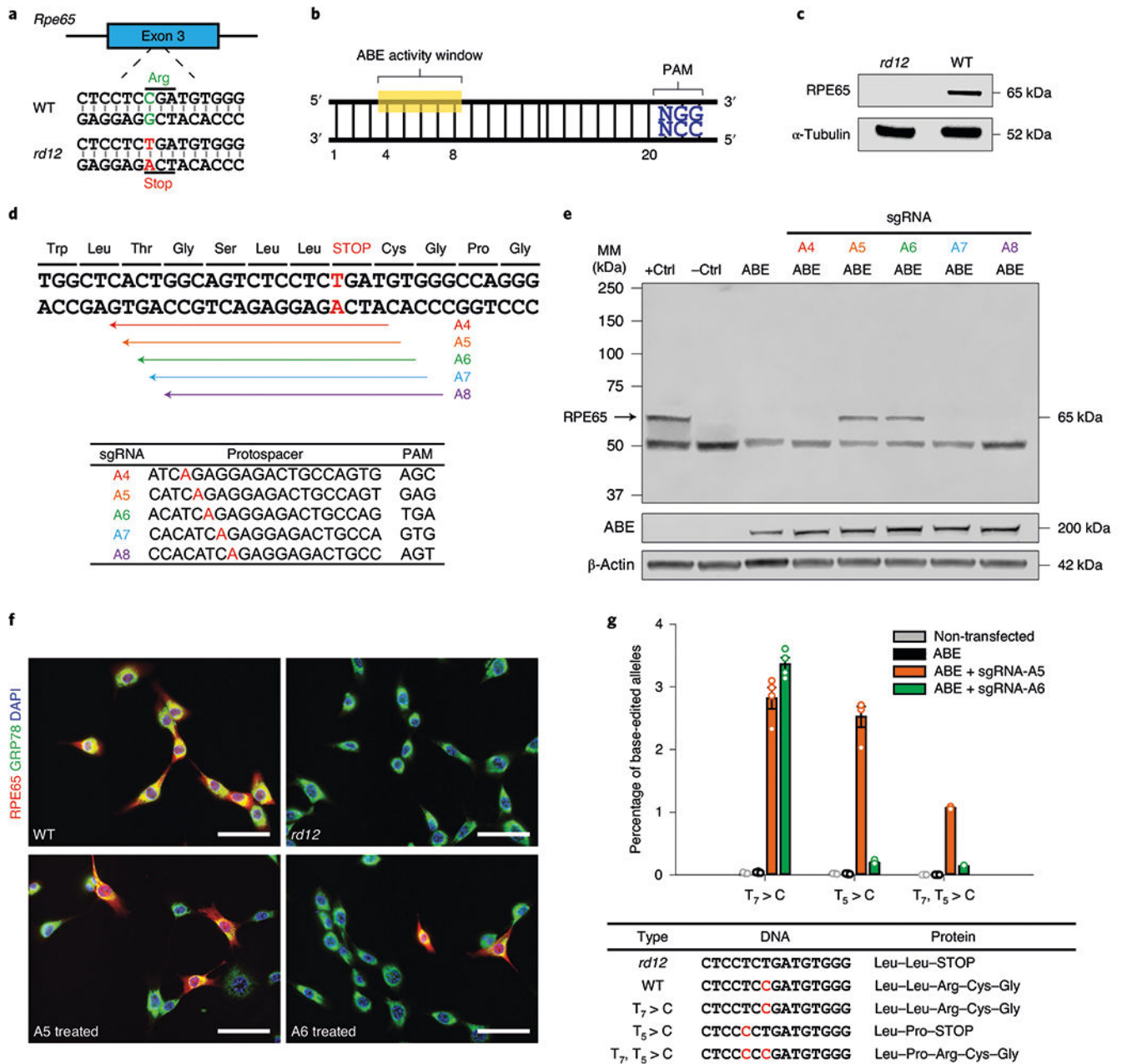
Fig. 1 |. In vitro validation of *Rpe65* mutation correction by the ABE.
a, The *rd12* mouse model has a homozygous C•G to T•A nonsense mutation in exon 3 of the *Rpe65* gene, changing arginine (green) to a stop codon (red). **b**, The ABE efficiently converts A to G in the genome that corresponds to a window of positions ~4-8 (yellow) in the guide RNA, counting the NGG PAM as positions 21-23. **c**, Validation of *rd12* (left lane) and WT (right lane) reporter cell lines by western blot analysis. The RPE65 band (65 kDa) is detected from the WT cell lysate but not from the *rd12* cell lysate. α-Tubulin (52 kDa) was used as a loading control. **d**, Five sgRNAs were designed to place the target mutation (red letter) within the ABE activity window. **e**, Western blot analysis of *rd12* cells following ABEmax and sgRNA plasmid transfection, showing the rescue of RPE65 protein with

sgRNA-A5 and sgRNA-A6. *rd12* cells transfected with pcDNA3.1 encoding WT mouse RPE65 were used as a positive control (+Ctrl). Non-transfected *rd12* cells were used as a negative control (−Ctrl). ABE (200 kDa) and β-actin (42 kDa) were used as loading controls. An additional band at 50 kDa has unknown identity but is irrelevant to RPE65 expression. MM, molecular mass. **f**, Immunocytochemistry of *rd12* cells transfected with sgRNA-A5 and sgRNA-A6 ($n = 3$ images from independent experiments), showing RPE65^{+} cells (red). Green indicates GRP78 and blue indicates DAPI staining. GRP78 served as a marker for endoplasmic reticulum localization. Scale bars, 50 μm. **g**, Deep sequencing of the target locus in *rd12* cells at 48 h post-transfection ($n = 4$ biologically independent replicates). Means ± s.e.m. are shown. The types of allelic variants are shown as DNA and translated amino acid sequences in the table. Allelic variants occurring at a frequency of <0.1% were not included in the analysis.
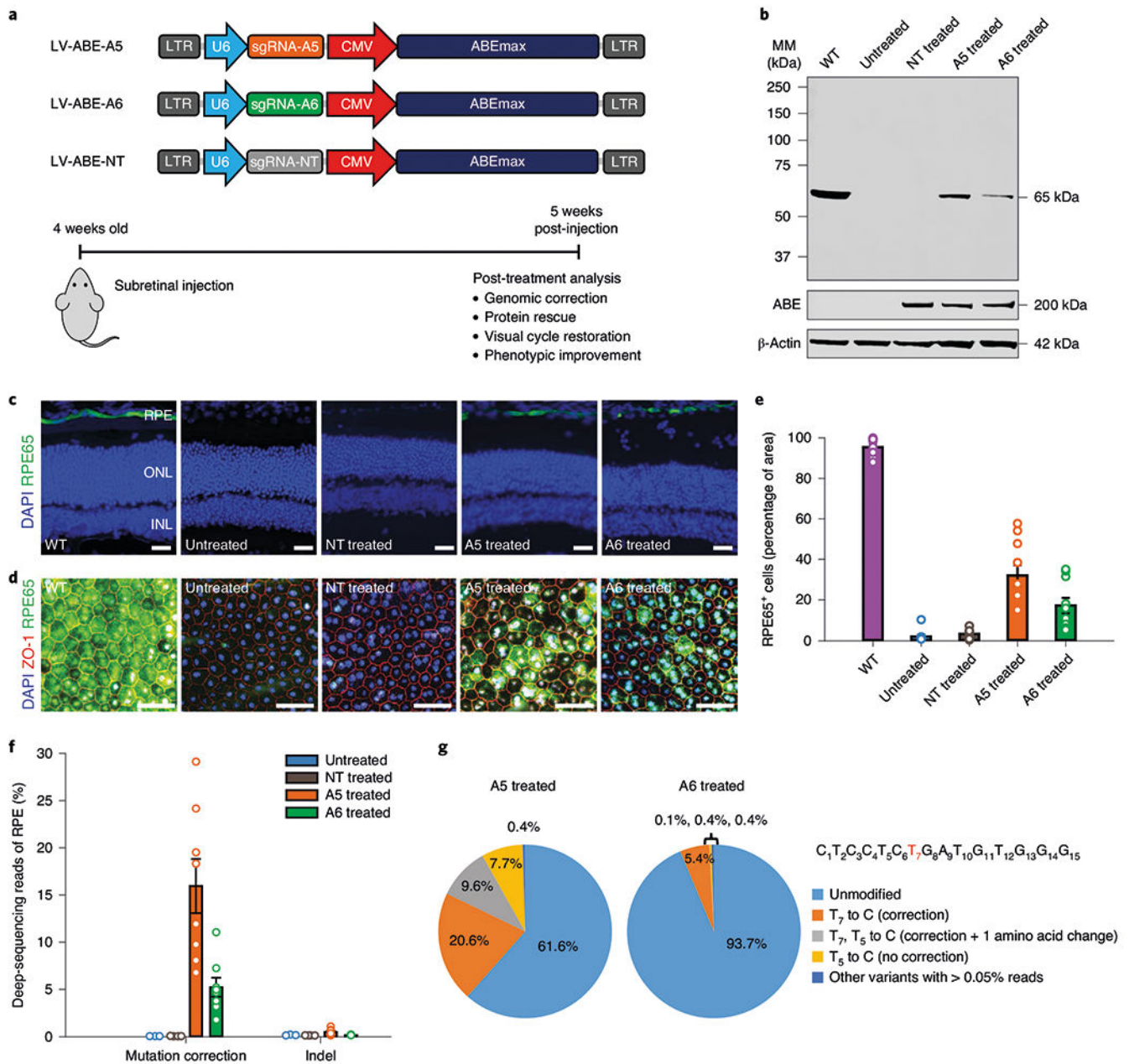
Fig. 2 |. Subretinal delivery of ABE corrects the mutation and restores RPE65 expression in *rd12* mice.

a, Schematic of three lentiviral vector genomes for subretinal delivery (top) and an outline of the in vivo experiments (bottom). LV-ABE-A5 and -A6 express the codon-optimized ABE (ABEmax) and sgRNA-A5 and sgRNA-A6, respectively. LV-ABE-NT is a control virus expressing ABEmax and non-targeting sgRNA. CMV, cytomegalovirus; LTR, long terminal repeat. **b**, Western blot analysis to detect RPE65 (65 kDa) expression from mouse RPE tissue lysate after treatment. Each lane represents a single eye with ~100% eGFP coverage. ABE (200 kDa) and β-actin (42 kDa) were used as loading controls. **c,d,** Immunofluorescence analysis of representative eye cross-sections (**c**) and RPE flatmounts

(**d**) of treated mice. Green indicates RPE65, blue indicates DAPI staining and red shows ZO-1 (a protein marker for tight junctions). Scale bars, 50 μm. INL, inner nuclei layer; ONL, outer nuclei layer. $n = 2$ images in **c** and $n = 3$ images in **d**. **e**, Quantification of RPE65+ cells from a single representative RPE flatmount, based on immunofluorescence ($n = 10$ images representing different areas). Means ± s.e.m. are shown. **f**, Deep-sequencing analysis of the *rd12* locus in genomic DNA isolated from the RPE tissue of untreated ($n = 3$ eyes), NT-treated ($n = 4$ eyes), A5-treated ($n = 8$ eyes) and A6-treated mice ($n = 8$ eyes). Means ± s.e.m. are shown. **g**, Pie charts showing the composition of allelic variants in one representative eye, for the A5 treatment (left) and the A6 treatment (right). Fifteen nucleotides spanning the target mutation (T_7) are shown as a reference using the unedited rd12 mouse sequence. Allelic variants with <0.05% reads were excluded. Unless otherwise noted, all post-treatment analyses were performed 5 weeks after subretinal injection using the mouse eyes that had >70% eGFP coverage.
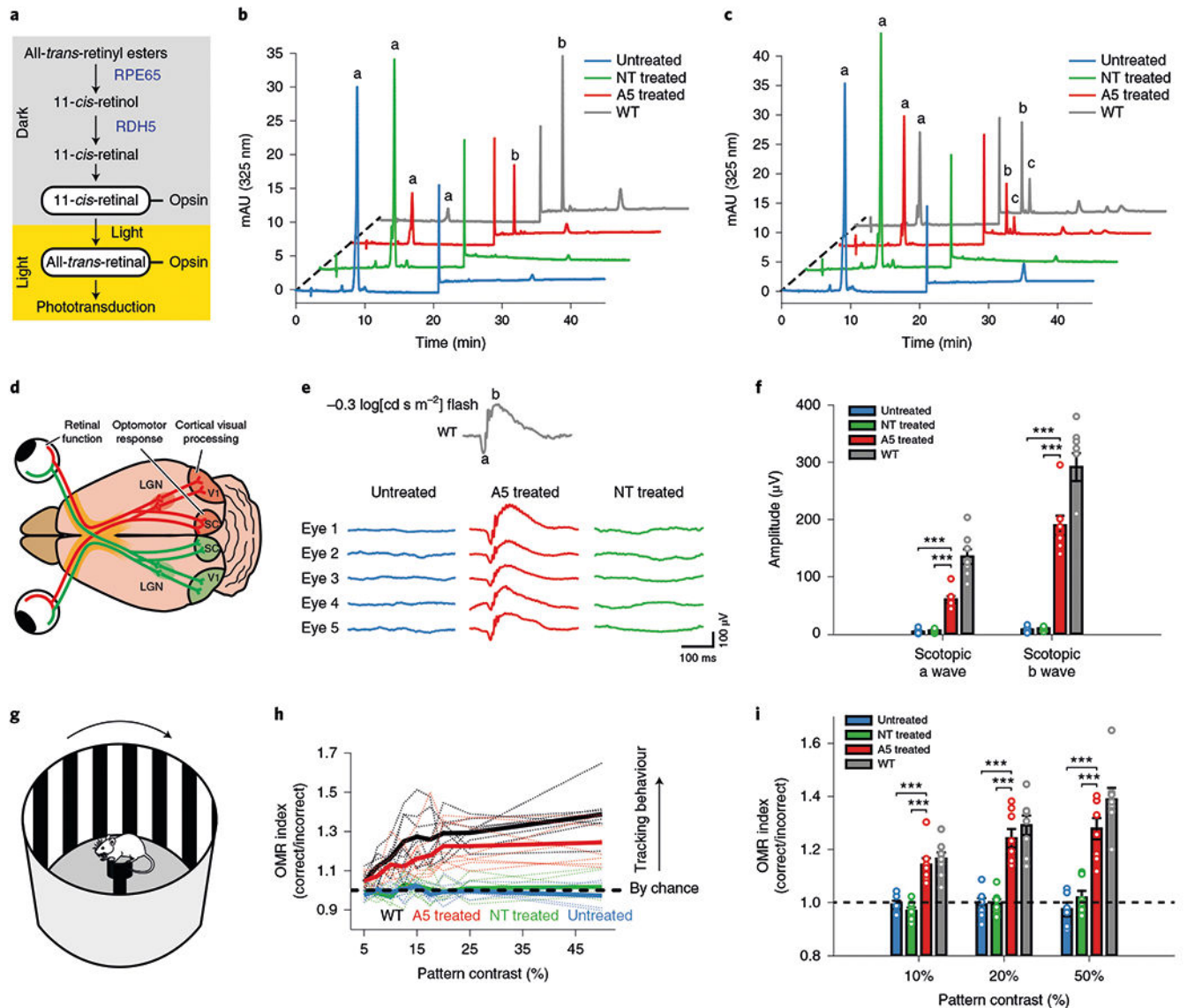
Fig. 3 |. Restoration of a visual cycle and retinal function in *rd12* mice after base editing.
a, Schematic of the visual cycle, demonstrating the enzymatic role of RPE65. RDH5, retinol dehydrogenase 5. **b,c**, Retinoid profiles of dark-adapted mouse eyes (**b**) and 0.5-s flash-bleached mouse eyes (**c**). Peak a, all-*trans*-retinyl esters; peak b, 11-*cis*-retinal; peak c, all-*trans*-retinal. Each chromatogram represents the homogenate from two eyes. **d**, Schematic of the visual pathway in the mouse. LGN, lateral geniculate nucleus; SC, superior colliculus; V1, primary visual cortex. **e**, Scotopic ERG waveforms of five mice from each group upon light stimulus of −0.3 log[cd s m^{-2}]. A representative waveform from one WT mouse is shown at the top. **f**, Measurements of scotopic a- and b-wave amplitudes by the ERG recordings in **e** ($n = 8$ mice in each group). Means ± s.e.m. are shown. ***$P < 0.001$ (one-way analysis of variance with Bonferroni test). **g**, Schematic of the OMR apparatus. A mouse is placed on an elevated platform where it can freely move and track the virtual rotating pattern stimulus displayed on the screen. Evaluation of head movements

synchronous to the stimulation is automated. **h,i**, Summary of OMRs at various pattern contrasts (**h**) and a comparison of average responses at 10, 20 and 50% pattern contrasts (**i**). An OMR index of 1 indicates head movements by chance. Statistically significant tracking was inferred using a one-tailed *t*-test based on a null hypothesis mean of 1 (**h**). Thin lines represent responses from individual animals. Thick lines represent average responses from each group. Numbers of mice were as follows: $n = 6$ (untreated); $n = 7$ (NT treated); $n = 8$ (A5 treated); and $n = 8$ (WT). The dashed horizontal line indicates an OMR index of 1. Means ± s.e.m. are shown. ***$P < 0.001$ (one-way analysis of variance with Bonferroni test).
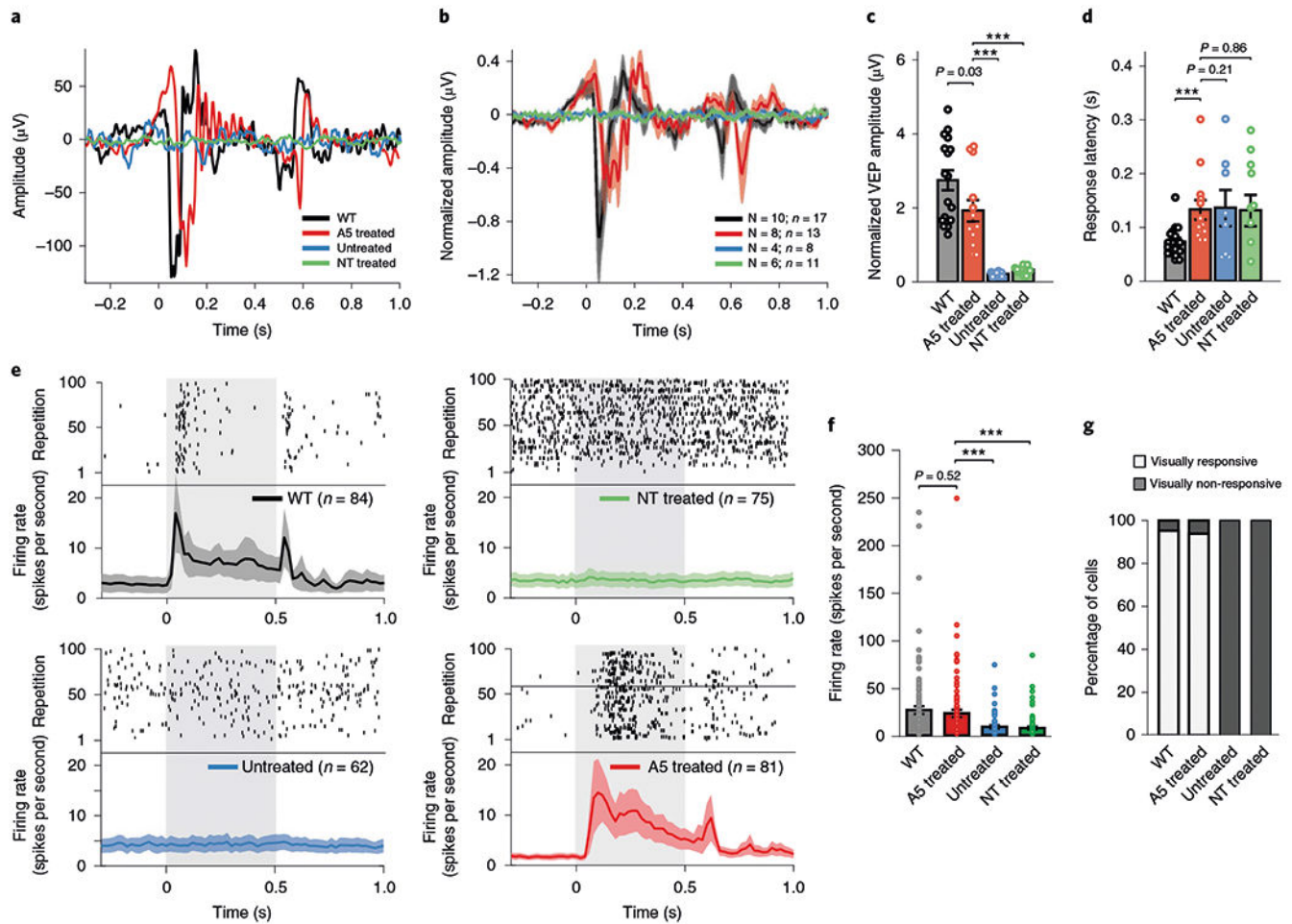
Fig. 4 |. Base editing restores neuronal activity of the primary visual cortex (V1) in response to visual stimuli.

a,b, Representative example of VEPs from a single mouse (**a**) and the average of normalized VEPs from each group (**b**). Shading indicates s.e.m. *N*, number of mice; *n*, number of recording sites. **c,d**, Population summaries of normalized VEP amplitudes (**c**) and response latency (**d**). Means ± s.e.m. are shown. ***$P < 0.001$ (two-tailed Mann-Whitney *U*-test). **e**, Flash-evoked single-neuron recordings from WT, untreated, NT-treated and A5-treated mice are shown as raster plots for single neurons (top) and as population averages (solid lines; bottom). Shading indicates s.e.m. The 500-ms duration of the flash stimulus is indicated by light grey background shading. Numbers of neurons (*n*) and mice (*N*) were as follows: $n = 84$ and $N = 10$ (WT); $n = 62$ and $N = 4$ mice (untreated); $n = 75$ and $N = 6$ (NT treated); and $n = 81$ and $N = 8$ mice (A5 treated). **f**, Summary of single-neuron firing rates from each group in response to flash stimuli. Means ± s.e.m. are shown. ***$P < 0.001$ (two-tailed Mann-Whitney *U*-test). **g**, Proportion of visually responsive and non-responsive single neurons in V1. Sample sizes for **f** and **g** match the numbers of neurons in **e**.
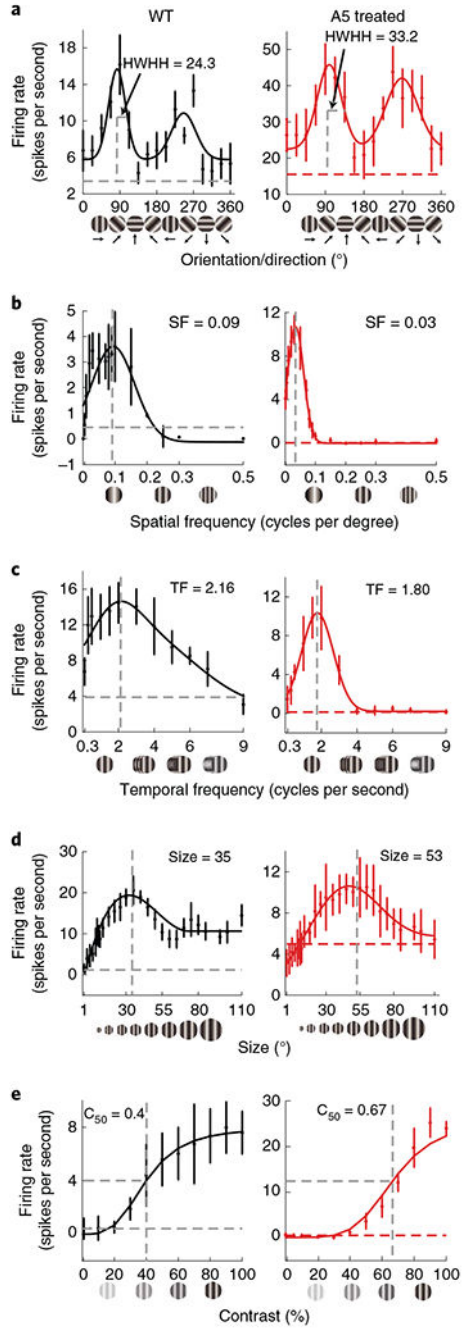
Fig. 5 |. V1 neurons in A5-treated mice show selectivity to stimulus parameters.
a–e, Comparisons of single-cell responses to different stimulus parameters between WT and A5-treated mice, including tuning curves for orientation (**a**), spatial frequency (**b**), temporal frequency (**c**), size (**d**) and contrast (**e**). Horizontal dashed lines indicate background activity, whereas vertical dashed lines indicate optimum stimulus parameters. C_{50}, percentage contrast at half of the peak response; HWHH, half-width at half height; SF, preferred spatial

frequency; TF, optimal temporal frequency; size, optimal stimulus diameter. Mean ± s.e.m. are shown.